Objective molecular dynamics study of cross slip under high-rate deformation

Gunjan Pahlani [a], Ananya Renuka Balakrishna [b], Richard D. James [a],*

[a] *Department of Aerospace Engineering and Mechanics, University of Minnesota, United States of America*
[b] *Materials Department, University of California, Santa Barbara, United States of America*

A R T I C L E   I N F O

A B S T R A C T

In this paper, we investigate high-strain-rate deformations in crystalline materials using a novel implementation of Objective Molecular Dynamics (OMD). The OMD method is exact and has a rigorous foundation based on the fundamental invariance of the underlying potential energy surface: all atoms out to infinity satisfy the equations of molecular dynamics to high accuracy. Using this OMD method, we compute how dislocations filling all of the space in a crystalline material undergo time-dependent, three-dimensional motions during deformation. We apply this method to investigate the dynamics of screw dislocations in FCC nickel. Our key finding is that the macroscopic motion (i.e., loading conditions) and initial conditions greatly affect the atomic scale deformation mechanisms—such as the formation, motion, multiplication, annihilation, and abrupt changes of the slip plane and Burgers vector of dislocations. Small changes in the macroscopic loading conditions generate a rich variety of atomic deformation pathways. In certain macroscopic motions, we observe the growth of a stacking fault into a mechanical twin, which subsequently thickens by a process of step motion. In other macroscopic motions, we observe the initiation and subsequent development of cross-slip by the Friedel–Escaig (FE) or Fleischer mechanisms (FL). Under mixed loading conditions, a novel mechanism, with a combination of both FE and FL mechanisms was also observed. Our findings on the effect of external strain rate and temperature on the critical stress for homogeneous cross-slip quantitatively agree with a version of transition state theory with a stress-dependent activation barrier. Beyond dislocation motion, we demonstrate the modeling of sliding surfaces using the OMD framework. These examples highlight potential applications of the OMD framework to the mechanisms underlying plastic deformation and friction in material systems.

1. Introduction

Molecular Dynamics (MD) is a powerful simulation technique that elucidates the macroscopic response of materials by exploring the dynamics of atoms at a microscopic scale (Alder and Wainwright, 1959). Despite its fundamental advantages, the MD approach suffers from two well-known limitations: its accessibility to only short time and length scales. For ergodic systems, in which the time evolution of a single atomic system is believed to be in statistical agreement with the evolution of a very large number of identical systems (ensemble) in phase space, these limitations are addressable to a certain extent. For example, periodic boundary conditions help to mitigate the length-scale limitations for bulk phenomena. With periodic boundary conditions, one surrounds the fundamental simulation domain by periodic images of itself which helps to remove finite-size/surface effects of the simulation

---

at modest additional computational cost (Allen and Tildesley, 2017). Similarly, Equilibrium Periodic MD (PMD) (that is linked to equilibrium statistical mechanics) is computed for different ensembles corresponding to various macroscopic boundary conditions imposed on the system. For example, a microcanonical ensemble corresponds to a system that is isolated with fixed total energy, a canonical ensemble corresponds to a system at a constant temperature, and a (generalized) stress ensemble corresponds to a system subjected to constant external stress. The simplest equilibrium molecular dynamics algorithm uses Hamilton's equations of motion alone, which would be appropriate for a microcanonical or adiabatic system. The other macroscopic constraints are achieved by imposing a thermostat and barostat on the system for a constant temperature/constant stress ensemble (Tadmor and Miller, 2011).

However, Non-Equilibrium Molecular Dynamics (NEMD) does not have a well-developed theoretical connection with a statistical mechanics framework, because of the absence of general non-equilibrium statistical mechanics. Thus, the use of equilibrium concepts of thermostat and barostat which are designed to sample the equilibrium probability density for tuning a system under far-from-equilibrium conditions is questionable since it can pollute the natural dynamics of atoms.

The method of Objective MD (OMD) generalizes PMD to non-equilibrium situations (Dayal and James, 2010; Aghaei and Dayal, 2011; Aghaei et al., 2013). It provides a framework to simulate a material under a family of macroscopic Lagrangian motions given by

$$\mathbf{y}(\mathbf{x}, t) = (\mathbf{I} + t\mathbf{A})\mathbf{x}, \tag{1}$$

where $\mathbf{A}$ is an arbitrary assigned 3×3 constant matrix, equal to the material time derivative of the deformation gradient tensor. This 9 parameter family of motions (Eulerian form: $\mathbf{v}(\mathbf{y}, t) = \mathbf{A}(\mathbf{I} + t\mathbf{A})^{-1}\mathbf{y}$) is quite simple but includes compressible and incompressible cases, time-dependent vorticity, and strong singularities at $t^\star$ in cases that $\det(\mathbf{I} + t\mathbf{A}) \to 0$ as $t \to t^\star$. Since all accepted models of materials in continuum mechanics (elastic/plastic, nonlinear elastic, Navier–Stokes, non-Newtonian, etc.) have the property that a motion with deformation gradient depending only on time has stress that depends only on time, then

$$\rho_0 \frac{\partial^2 \mathbf{y}}{\partial t^2} = \operatorname{div} \boldsymbol{\sigma} = 0, \ \ \boldsymbol{\sigma} = \bar{\boldsymbol{\sigma}}(t) \tag{2}$$

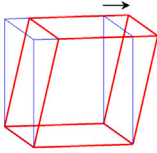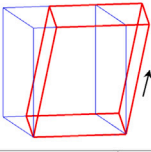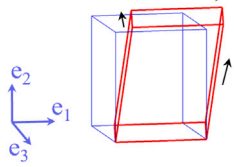is satisfied by all materials in this case.

Thus, the motions we study have zero macroscopic inertia. The invariance of the atomic forces of MD give rise to "universal motions" which satisfy momentum conservation of continuum mechanics for all accepted constitutive models (Dayal and James, 2012). This synergy encourages the use of OMD to build higher-scale models. One such effort is to develop a non-classical constitutive model for universal flows of dilute gases which improves Navier–Stokes prediction under strong gradients (Pahlani et al., 2022b, 0000).

Essentially, what we realized in research leading to this paper is that, even in highly inhomogeneous cases such as complex dislocation motion or frictional sliding, where we are far from having an accepted macroscopic constitutive equation, the method of OMD remains a useful tool to learn about the dynamic behavior of materials.

In OMD, one considers a set of atoms (simulated atoms) denoted by $\mathbf{y}_k(t)$, $k = \{1, \ldots, M\}$, and the MD equations are satisfied for those atoms. The motions of all the other infinite (non-simulated) atoms are obtained by exploiting the basic invariance of quantum mechanics. More precisely, the positions of the non-simulated atoms are given by elements of a time-dependent discrete group of isometries acting on the simulated atoms. The main result is that every atom satisfies the MD equations exactly for its forces, even though these equations are not being solved for non-simulated atoms explicitly. The advantage is that the dynamics of atoms is exact and hence is applicable in the far-from-equilibrium regime. There exist many choices of isometry groups that provide an exact NEMD approach for various systems ranging from nano-structures to bulk systems (Aghaei et al., 2013; Pahlani et al., 2022b). In this paper, the group is specialized to be the time-dependent translation group (TDTG), which gives rise to macroscopic motions of the form (1). The computational design of OMD corresponding to TDTG is provided in earlier work (Pahlani et al., 2022a).

Generally, the simulated atoms can lie anywhere in space. They can also be chosen to lie in a fundamental domain of the group, in which case the connection with the periodic boundary conditions becomes more apparent. As in periodic boundary conditions, if a simulated atom leaves the fundamental domain, then a corresponding nonsimulated atom enters that domain, but, unlike PMD which describes the system under adiabatic conditions, this nonsimulated atom enters with a different velocity. The relationship between the trajectory of non-simulated and simulated atoms is provided in Section 2. Also, the fundamental domain deforms in time and its motion is given by (1). All atoms, both inside and outside the deforming fundamental domain, satisfy exactly the equations of molecular dynamics for their forces. The macroscopic motion associated with TDTG of OMD corresponds to the application of a macroscopic boundary condition of constant engineering strain rate to the material. In the literature, there are computational tools corresponding to the application of true strain rate (Thompson et al., 2022) as well. To our knowledge, unlike OMD, these simulations cannot be extended to larger domains as exact solutions, but better represent small-volume behavior under these boundary conditions.

Another widely used method to conduct NEMD simulations imposes explicit external forces in the equation of motion in conjunction with periodic boundaries to achieve any desired homogeneous motion. The method was pioneered by Hoover and Evans and is considered suitable for fluid flows (Hoover et al., 1980; Evans and Morriss, 1984). Because of the fictitious forces, we doubt it would give results in any way similar to those of OMD and sample the non-equilibrium distribution corresponding to it, even in cases where the homogeneous motion matches the average motion of OMD. In other words, we find a significant dependence of behavior on the specifics of atomic forces. In the special case of simple shearing motion, OMD is formally the same as early nonequilibrium simulations of shear flow by Lees and Edwards (1972). However, it is our opinion that the use of moving boxes

Isochoric motions **A**   Reference/Deformed configuration

Simple Shear

$$\begin{bmatrix} 0 & K_1 & 0 \\ 0 & 0 & 0 \\ 0 & 0 & 0 \end{bmatrix}$$

Orthogonal Shear 1

$$\begin{bmatrix} 0 & K_1 & K_2 \\ 0 & 0 & 0 \\ 0 & 0 & 0 \end{bmatrix}$$

Orthogonal Shear 2

$$\begin{bmatrix} 0 & K_1 & K_2 \\ 0 & 0 & K_3 \\ 0 & 0 & 0 \end{bmatrix}$$

e_2 e_1 e_3

Fig. 1. A list of isochoric motions and schematic illustrations of the corresponding deformations of an orthonormal cubic cell. We simulate these motions as affine deformation of the unit cell in the OMD framework. The deformations have been exaggerated for illustration purposes.

as in the work by Lees and Edwards method is not an efficient implementation and apparently does not extend to the many other possible choices of **A** besides simple shearing. By contrast, we can simulate a range of shear deformations using OMD as illustrated in Fig. 1.

In summary, the OMD method used here is an exact method of molecular dynamics. The system is not in statistical equilibrium and the phase space distribution function is time-dependent. Also, the Hamiltonian of any subset of atoms is far from being constant. The simulations can be highly dissipative, especially when dislocations are moving, and the temperature changes in time.

In this study we focus on the usage of OMD for problems in materials science, particularly for the investigation of the dynamics of dislocations. We also illustrate its potential for problems involving friction, also using the translation group. In our recent work (Pahlani et al., 2022a) we modeled families of incompressible, compressible, and unsteady flows in Lennard-Jones systems. The macroscopic flows predicted by OMD were shown to be the exact solutions of the Navier–Stokes equations. This exact modeling framework (i.e., same numerics, macroscopic deformations (same **A**)) is applied in the current work to a crystalline material with different inter-atomic potential and initial conditions, to investigate the evolution of dislocations and friction at the atomic scale. In fact, exactly the same computer program can be used for fluids and dislocations, although the efficiency of the method depends on the details of the implementation. Thus, OMD is a universal NEMD approach for investigating the non-equilibrium dynamics behavior of the system.

Dislocations are important defects of crystals that are a primary microscopic mechanism of plasticity. Thus the study of their dynamic behavior is important for a complete understanding of plastic deformation in crystalline materials. Plasticity is characterized by phenomena occurring across several orders of magnitude in length and time scales (Tadmor et al., 1996; Tadmor and Miller, 2011; Conti et al., 2007) which makes it complicated to segregate the role played by different phenomena in guiding the particular macroscopic behavior.

In this work, we focus on the atomistic length scale and investigate the phenomenon of cross-slip, a fundamental aspect of the motion of screw dislocations (Hull and Bacon, 2001). Cross-slip in close-packed lattices will influence the behavior and arrangement of dislocations on a mesoscopic scale which can affect macroscopic behavior. The microscopic investigation conducted in this study can assist the modeling of cross-slip at the mesoscopic scale within the framework of dislocation dynamics simulation under high-rate loading conditions.

Fundamentally, cross-slip provides an extra degree of freedom for the motion of a screw dislocation (Kubin, 2013), whereby a screw dislocation can leave its habit plane and glide in a conjugate "cross-slip" plane. It plays a crucial role in phenomena like work hardening, recovery, fatigue, creep, and pattern formation, Püschl (2002) and Madec et al. (2002). Microscopically, cross-slip enables the annihilation of dislocations of opposite Burgers vector and also allows the passing of dislocations around obstacles such as precipitates or inclusions present in the dislocation path. Cross-slip is typically associated with Stage III hardening in FCC metals; however occasional cross-slip can also happen in other stages. Hence, its role as a softening or hardening mechanism depends on the details of its occurrence. Therefore, it is important to have complete predictability on the critical stress of cross-slip under given loading conditions.

As in most microscopic phenomena associated with plasticity, cross-slip is a thermally activated process. Small groups of atoms hop from one metastable state to another with a rate that depends on the mechanism as well as the temperature and stress. Studies in the literature have often focused on a system under constant stress and temperature to study the kinetics and kinematics of a

cross-slip event (Esteban-Manzanares et al., 2020; Oren et al., 2017). At the atomic scale, this is achieved by using statistical NσT ensemble based on the Parrinello and Rahman stress control method and the Nose Hoover thermostat and its variants, whose aim is to sample the time-invariant equilibrium probability distribution at constant stress and temperature (Parrinello and Rahman, 1981; Miller et al., 2016). This is analogous to quasi-static loading where the system follows near-statistical equilibrium behavior. But in experiments, approximately constant strain rate and evolving temperature are quite common. In addition, the study of cross-slip dynamics under extreme loading conditions is equally important and is less well understood. In this work, we use the approach of OMD to investigate this regime where the system is far-from-equilibrium.

The paper is organized as follows: in Section 2 we briefly explain the method of OMD. In Section 3 we discuss the computational setup and report various mechanisms of cross-slip in the regime of high-rate deformation. We investigate the choice of the tensor **A** (macroscopic motion) on dislocation evolution for smaller and flexible dislocation segments. Later, we assess the applicability of transition state theory (TST) under highly non-equilibrium conditions. It is surprising to us that there is some level of agreement between a modified version of TST and our simulations. We do not see persuasive evidence of atoms entering a well, equilibrating, and then passing out of a well through a low barrier in the simulations. In Section 4 we show the flexibility of the OMD framework to study sliding behavior. Finally, the conclusions are contained in Section 5.

2. Objective molecular dynamics

Equilibrium statistical mechanics is based on a time-independent invariant manifold defined by $H = const.$, where H is the Hamiltonian. On the other hand, Objective Molecular Dynamics (OMD) is a simulation approach based on an explicit but time-dependent invariant manifold of MD equations defined by (6) below. The manifold has dimension $(6N + 1)$. The existence of this invariant manifold follows from key properties of frame-indifference and permutation invariance of the potential energy, together with the fact that the kinetic energy is quadratic in the velocities (Dayal and James, 2012). These properties offer a generalized and vast manifold that is exploited in OMD. In this section, we provide a brief overview of the Objective Molecular Dynamics approach and identify its distinguishing features making it a suitable simulation approach to study dislocation dynamics and friction in crystalline materials. For a detailed overview of the OMD method see Dumitrică and James (2007).

2.1. Potential energy

In the OMD framework, we index atom positions $\mathbf{y}_{i,k}$ by the double index (i, k) where $i = 1, \dots, N, \ k = 1, \dots, M$. In applications presented in this paper using the translation group, $N = \infty$; for finite groups N is finite and in that case N/k must be chosen as an integer. Atoms with the same second index, e.g., (i_1, k) and (i_2, k), must necessarily be the same species. Frame indifference – invariance of the potential energy under orthogonal transformation, translation and permutation – under the Born–Oppenheimer approximation of quantum mechanics is given by

$$\varphi(\dots, \mathbf{y}_{i_1,1}, \dots \mathbf{y}_{i_1,M}, \dots, \mathbf{y}_{i_2,1}, \dots \mathbf{y}_{i_2,M}, \dots)$$
$$= \varphi(\dots, \mathbf{Q}\mathbf{y}_{i_1,1} + \mathbf{c}, \dots \mathbf{Q}\mathbf{y}_{i_1,M} + \mathbf{c}, \dots, \mathbf{Q}\mathbf{y}_{i_2,1} + \mathbf{c}, \dots \mathbf{Q}\mathbf{y}_{i_2,M} + \mathbf{c}, \dots)$$
$$= \varphi(\dots, \mathbf{y}_{\Pi(i_1,1)}, \dots \mathbf{y}_{\Pi(i_1,M)}, \dots, \mathbf{y}_{\Pi(i_2,1)}, \dots \mathbf{y}_{\Pi(i_2,M)}, \dots), \tag{3}$$

where $\mathbf{y}_{i,k}$ represents the position of atom (i, k), $\mathbf{Q}$ is a tensor in O(3), $\mathbf{c}$ is a translation in $\mathbb{R}^3$ and $\Pi(\cdot, k)$ is a permutation on its first index of $1, \dots, N$ for each k. Put simply: the positions of atoms of the same species can be interchanged without affecting the potential energy. These invariances can also be written for the forces acting on atoms by formally differentiating (3) with respect to positions of atoms. The latter still holds in cases that the potential energy is infinite, which occurs in the present case.

2.2. Objective structures

The invariance of the atomic forces is closely associated with the underlying long-range symmetries of various special structures called objective structures (James, 2006) and a family of flows termed universal flows (Dayal and James, 2012). The symmetry of interest here is represented by a time-dependent isometry group $\mathcal{G}^{(t)} = \{g_1^{(t)}, \dots, g_N^{(t)}\}$, $1 \le N \le \infty$, i.e., groups of orthogonal transformation and translations in which the translation is affine in time. The action of its elements on a point $\mathbf{y} \in \mathbb{R}^3$ is given by

$$g_i^{(t)}(\mathbf{y}) = \mathbf{Q}_i \mathbf{y} + \mathbf{c}_i^{(t)}; \qquad g_i^{(t)} = (\mathbf{Q}_i | \mathbf{c}_i^{(t)})$$

$$\mathcal{G} = \{g_1^{(t)}, g_2^{(t)}, \dots, g_N^{(t)}\}, \ g_1^{(t)} = g_1 = id, \tag{4}$$

where the $\mathbf{c}_i^{(t)}$ are affine in time. The group product is the standard one for isometries: $(\mathbf{Q}_1|\mathbf{c}_1)(\mathbf{Q}_2|\mathbf{c}_2) = (\mathbf{Q}_1\mathbf{Q}_2|\mathbf{c}_1 + \mathbf{Q}_1\mathbf{c}_2)$. The inclusion of time dependence makes this an exact NEMD method in the framework of OMD. Here, the equations of MD are solved for *M simulated atoms* $\mathbf{y}_{1,j}$, $j = 1, \dots, M$ and the trajectory of all the other (typically infinitely many) non-simulated atoms are obtained by applying isometry groups to the set of simulated atoms using the rule given in (4):

$$\mathbf{y}_{i,j} = g_i^{(t)}(\mathbf{y}_{1,j}), \quad i = 2, 3, 4 \dots. \tag{5}$$

In previous work (Dayal and James, 2010), it is proved that mapping the trajectory of infinitely many non-simulated atoms $\mathbf{y}_{(i,j)}$ using Eq. (5) provides the necessary and sufficient conditions for non-simulated atoms to satisfy the equations of molecular dynamics for their forces (provided that the simulated atoms also obey the MD equations). This is obtained by exploiting the special structure of the equations of molecular dynamics as noted above.

2.3. Time-dependent translation group

While there is tremendous latitude for choosing groups and (affine) time dependencies, we will confine attention in this paper to the pure translation group $\mathbf{Q}_i = \mathbf{I}$, $i = 1, \ldots, N$. In this case a useful relabeling of the group is to replace the single index i by a triple of integers $\nu = (\nu^1, \nu^2, \nu^3)$ with M simulated atoms denoted $((0,0,0), k)$, $k = 1, \ldots, M$. In this case the group is $\mathcal{G}^{(t)} = \{(\mathbf{I} | \nu^1(\mathbf{I} + t\mathbf{A})\mathbf{e}_1 + \nu^2(\mathbf{I} + t\mathbf{A})\mathbf{e}_2 + \nu^3(\mathbf{I} + t\mathbf{A})\mathbf{e}_3) : \nu^{1,2,3} \in \mathbb{Z}\}$, where $\mathbf{e}_1, \mathbf{e}_2, \mathbf{e}_3$ are given linearly independent vectors, and $\mathbf{A}$ is a linear transformation. Clearly, this is a group under the product rule given above, and it has the affine time-dependence. The relation between the positions and velocities of simulated and non-simulated atoms is then

$$
\begin{aligned}
\mathbf{y}_{\nu,j} &= g_\nu^{(t)}(\mathbf{y}_{(0,0,0),j}(t), t) \\
&= \mathbf{y}_{(0,0,0),j}(t) + \nu^1(\mathbf{I} + t\mathbf{A})\mathbf{e}_1 + \nu^2(\mathbf{I} + t\mathbf{A})\mathbf{e}_2 + \nu^3(\mathbf{I} + t\mathbf{A})\mathbf{e}_3
\end{aligned}
$$

$$
\mathbf{v}_{\nu,j} = \mathbf{v}_{(0,0,0),j}(t) + \nu^1\mathbf{A}\mathbf{e}_1 + \nu^2\mathbf{A}\mathbf{e}_2 + \nu^3\mathbf{A}\mathbf{e}_3, \tag{6}
$$

respectively. When $\mathbf{A} = \mathbf{0}$, OMD reduces to conventional periodic molecular dynamics (PMD) describing the system under adiabatic conditions, where the total energy of the system is conserved and the velocity of non-simulated $\mathbf{v}_{\nu,j}$ and simulated atoms $\mathbf{v}_{(0,0,0),j}$ become equal. Thus, the method of Objective Molecular Dynamics generalizes the periodic molecular dynamics to non-equilibrium situations in an exact manner where each atom in the system satisfies Newton's equation of motion for its forces.

The proof that each of the infinitely many non-simulated atoms satisfies the MD equations for its forces uses the frame-indifference and permutation invariance (i.e., switching positions of like species) of the atomic forces, and the fact that the kinetic energy is quadratic in the velocities (Dayal and James, 2010).

2.4. Isochoric motions

To explain the method in a simpler context, Fig. 2 illustrates the method for general incompressible motion of Lennard Jones argon with dislocations in a defective lattice where $\mathbf{A}$ is given by $\mathbf{A} = \kappa\mathbf{e}_1 \otimes \mathbf{e}_2$ and $\mathbf{v}(\mathbf{x}, t) = \mathbf{A}(\mathbf{I} + t\mathbf{A})^{-1}\mathbf{x}$ with orthonormal vectors $\mathbf{e}_1, \mathbf{e}_2, \mathbf{e}_3$. Here, simulated atoms (cyan and orange atoms) lie in a fundamental domain (parallelepiped defined by $\mathbf{e}_1$, $\mathbf{e}_2$ and $\mathbf{e}_3$) at $t = 0$. With $\mathbf{A} \neq \mathbf{0}$, the initially defined domain starts deforming under the macroscopic motion. Due only to MD simulation, the simulated atoms leave the domain as time evolves under the influence of forces from other simulated and nonsimulated atoms. At any instant, the positions of simulated atoms can be used to find corresponding non-simulated atoms using (6). The non-simulated atoms fill all of the space but, for clarity, in Fig. 2, nonsimulated atoms are not shown. The simulated atoms are colored based on their coordination (cyan is FCC and orange is HCP) with lower transparency of atoms not lying on the center slice of the domain. Note that isochoric motion illustrated here is accomplished by a special choice of the components of the matrix $\mathbf{A}$ out of many other possibilities available. While we focus on isochoric macroscopic motions in this work, the method is not restricted to that case. For example, the well-known pressure–shear plate impact (PSPI) experiment corresponds approximately to a choice of $\mathbf{A}$ given by $\mathbf{A} = -K_1\mathbf{e}_1 \otimes \mathbf{e}_1 + K_2\mathbf{e}_1 \otimes \mathbf{e}_2$ (Kim and Clifton, 1980; Abou-Sayed et al., 1976; Ravindran et al., 2020).

3. Screw dislocations

3.1. Initialization

In this case, screw dislocations are introduced into the initial conditions for the simulated atoms of Ni, which are otherwise in a relaxed FCC structure. The interatomic interaction is described by an embedded-atom method (EAM) potential developed by Rao et al. (1999) using the Voter and Chen format (Voter and Chen, 1986). Table 1 lists the lattice parameter, cohesive energy, elastic constants and stacking fault energy for the potential. The correct prediction of the stacking fault energy (SFE) which is defined as the energy cost per unit area for changing the local stacking of the fcc {111} planes from ABCABC to ABC|BCA is especially important for dislocation related mechanisms. This force field gives good agreement between experiment and theory for the SFE (Siegel, 2005; Bernstein and Tadmor, 2004).

To construct the initial atomic configuration, we use the Atomsk package (Hirel, 2015). The atoms are assigned random initial velocities extracted from a Maxwell–Boltzmann distribution at a given temperature T. Two perfect screw dislocations with opposite Burgers vectors $\pm\mathbf{b}$ are introduced into the domain along the $\mathbf{e}_2$ axis to maintain a net Burgers vector of zero, so as to be consistent with the approximate periodicity of the surrounding lattice. This is to ensure the continuity in the displacement field along the edges of the computational domain so that time-dependent periodicity in OMD is maintained. The screw dislocations are located on parallel $(\bar{1}11)$ planes as shown in Fig. 3. Note that the dislocations generated by Atomsk are not relaxed. They correspond to the displacement fields predicted by anisotropic elasticity theory for a given set of material properties. To equilibrate them, we simulate the system under $\mathbf{A} = \mathbf{0}$ before applying any motion to the domain. This is equivalent to periodic MD at macroscopic equilibrium.

Fig. 3 shows the initial state of two screw dislocations. Cyan colored atoms shown there are in FCC coordination. Starting with a rectangular atomic cell, defined by vectors $\mathbf{e}_1, \mathbf{e}_2$ and $\mathbf{e}_3$ at $[1\bar{1}2]$, $[\bar{1}11]$ and $[110]$, respectively, we first generate a dipole of infinite straight parallel perfect screw dislocations, $\mathbf{b} = \frac{a_0}{2}[110]$ (shown as the blue dislocation lines in Fig. 3(a)). The orientations of the domain are chosen such that the axes correspond to the glide plane $(\bar{1}11)$ and glide direction $[1\bar{1}2]$. Equilibration under the NVE ensemble then leads to splitting of the perfect dislocation into the cores of the two Shockley partials identified by Burgers vectors
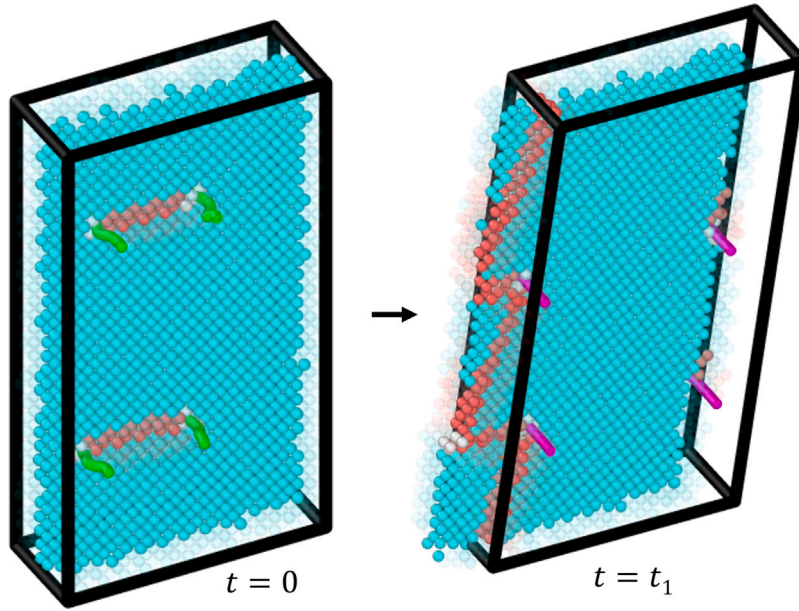
Fig. 2. Illustration of a three-dimensional isochoric motion ($\mathbf{A} = K_1 \mathbf{e}_1 \otimes \mathbf{e}_2$). The fundamental domain (22.9 Å × 43.2 Å × 8.8 Å) deforms under the macroscopic motion. The parallelepipeds represent the macroscopic motion, but atoms move in and out of these parallelepipeds according to the OMD method, as seen at $t = t_1$. The transparency of atoms not lying on the center plane has been reduced for better illustration. Different colored atoms depict different coordination and line vectors show dislocations.

$\mathbf{b}_1$, $\mathbf{b}_2$ and with an intervening stacking fault in accordance with the energetic argument provided by Frank's rule, Fig. 3(b) and (c). The screw dislocations can have different equilibrium core structures which can lead to splitting of screw dipoles on either glide ($\bar{1}11$) or cross-slip (111) planes creating 4 possible combinations. We choose the first case where both partials reside on glide plane as our starting point. This equilibrated configuration is then further used to perform non-equilibrium OMD simulations. The OVITO package is used for visualizations provided in this work (Stukowski, 2009).

In the simulations, dislocations fill all of space. The use of OMD results in an infinite array of dislocation dipoles which gives rise to image forces. We systematically varied the sizes of the fundamental domains and ran preliminary simulations to examine the effect of these forces: the simulation cell was increased in the in-plane directions $\mathbf{e}_1$ and $\mathbf{e}_2$ keeping the dislocation line length constant. Table 2 lists domain sizes for the different cases considered. These have a high aspect ratio of the fundamental domain. This feature was also found to mitigate the effects of image and dipole interaction forces based on atomistic investigation (Oren et al., 2016). From prior work, Mordehai et al. (2003) the contribution of these forces was found to be insignificant if the externally applied stress σ_{ext} is greater than $\sigma_c = \frac{\mu b L}{8\pi^2 r_0^2}$. For the smallest domain we have considered, $\sigma_c = 7.9$ MPa which is three orders of magnitude smaller than the dominant peak external stress applied to the domain.

Dislocations are identified in atomistic simulations performed here using the Dislocation Extraction Algorithm (DXA) implemented in the OVITO package (Stukowski and Albe, 2010). The DXA algorithm constructs Burgers circuits to find the existing dislocations. The correct search space is identified using Common Neighbor analysis which locates atoms that form a perfect (but elastically strained) crystal lattice. We find that the width of the stacking faults constantly fluctuates, governed by a balance between elastic and thermal forces. This known phenomenon is termed dislocation breathing in Mordehai et al. (2005).

Our OMD simulations focused on simple shear of bulk crystalline materials is conducted by adapting the classical molecular dynamics simulator LAMMPS. "Fix deform" with style "erate" is used to apply "constant engineering strain rate" to the material. It is accommodated with keyword "remap" for positions and velocities. This is to enable use of the relationship (6) to find the trajectory of a nonsimulated atom that enters the fundamental domain as its corresponding simulated atom exits. It is essential to redefine the non-simulated atoms entering the domain as simulated atoms to be consistent with the OMD method. (This corresponds to the redefinition defined in Pahlani et al. (2022a)). The box motion is updated at every time step and the velocity Verlet algorithm is used to integrate the Newton's equations of motion with a time step of 1 fs. We note that the Velocity Verlet algorithm perfectly matches the structure of OMD at discrete level: the non-simulated atoms exactly satisfy the Velocity Verlet algorithm for their neighbors, if the simulated atoms are subject to this algorithm.

3.2. Effect of external loading on cross slip mechanism

We use simple shearing motion along various directions to explore the effect of different components of stress on the detailed dislocation reactions during dynamic evolution. We investigate different mechanisms of cross-slip by varying the stress state in the

Table 1

Lattice parameter, elastic constants, cohesive energy and stacking fault energy given by the Ni EAM "vnih" potential.

Property	Value
a_0 (nm)	0.3526
c_{11} (N/m^2)	2.44×10^{11}
c_{22} (N/m^2)	1.49×10^{11}
c_{44} (N/m^2)	1.19×10^{11}
E_c (eV)	−4.43
γ (J/m^2)	0.119

Table 2

Different choices of the size of fundamental domain and number of simulated atoms N.

Domain	Dimension (a_1 Å × a_2 Å × a_3 Å)	N
(1)	(77.6 × 304.8 × 19.9)	43 200
(2)	(142.27 × 353.61 × 19.9)	91 872
(3)	(107.8 × 353.6 × 79.6)	278 400
(4)	(142.27 × 353.6 × 82.13)	378 972
(5)	(142.27 × 353.61 × 149.335)	689 040
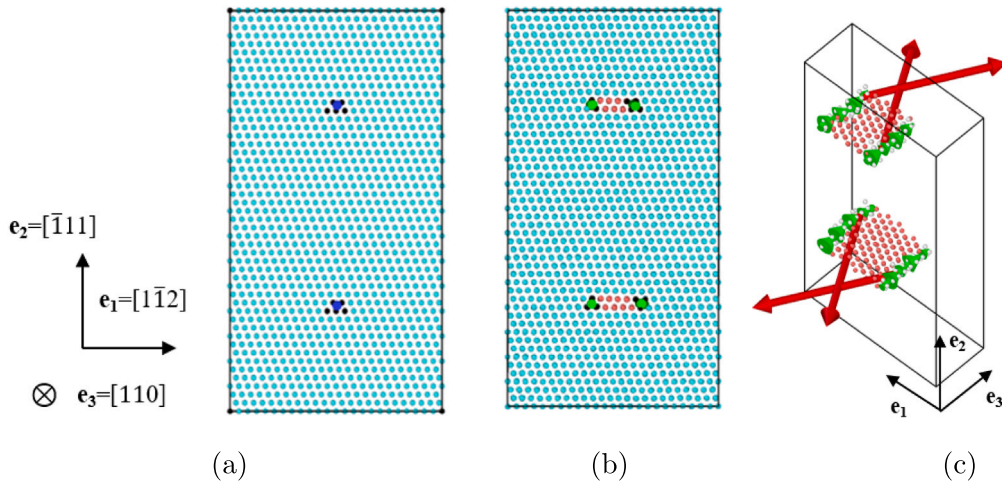
Fig. 3. (a) We initialize a fundamental domain with the cyan-colored atoms in FCC coordination. To this domain, we introduce two perfect screw dislocations (depicted by blue lines) on $(\bar{1}11)$ planes. (b) On equilibration, the screw dislocations dissociate into Shockley partial dislocations (depicted by green lines) with an intervening stacking fault. The red atoms are now in HCP coordination. (c) We illustrate the atomic arrangement in the vicinity of Shockley partial dislocations and the red vectors depict Burgers vectors of these dissociated partials.

material. The external loading is characterized using two definitions of stress: Escaig and Schmid stress. Stress that acts on the edge component of a Shockley partial dislocation and controls its width is referred to as Escaig stress and the one which interacts with screw component is referred to as the Schmid stress. These same definitions hold for both glide and cross-slip planes (Esteban-Manzanares et al., 2020; Kuykendall et al., 2020). These stresses are given in terms of stress components in $\mathbf{e}_1, \mathbf{e}_2, \mathbf{e}_3$ coordinate system as follows:

$$\sigma_s^g = \sigma_{23}, \qquad \sigma_s^{cs} = \sin\theta \sigma_{13} - \cos\theta \sigma_{23},$$
$$\sigma_e^g = \sigma_{12}, \qquad \sigma_e^{cs} = \cos 2\theta(\sigma_{12}) + \frac{\sin 2\theta}{2}(\sigma_{11} - \sigma_{22}), \tag{7}$$

where, θ is the angle between primary and cross-slip plane, subscripts 'e' and 's' refer to Escaig and Schmid, and superscripts 'g' and 'cs' refer to glide and cross-slip plane, respectively.

The correct atomistic definition of stress under non-equilibrium conditions is an actively studied subject. Different definitions used in the literature have been unified by Admal and Tadmor (2010). They find that the Hardy stress tensor has many favorable features under non-equilibrium conditions, assuming that the system is in local thermodynamic equilibrium. Also the Hardy stress is equivalent to the virial stress when a constant weighting function over the entire fundamental domain is used for the averaging (Hardy, 1982; Hardy et al., 2002). This definition is used below to compute a pointwise uniform instantaneous stress which is composed of kinetic and virial contributions. These pointwise values are then averaged over an ensemble of OMD trajectories (random momentum at given initial temperature T is assigned to each atom using a fresh random number seed) to compute macroscopic stress.
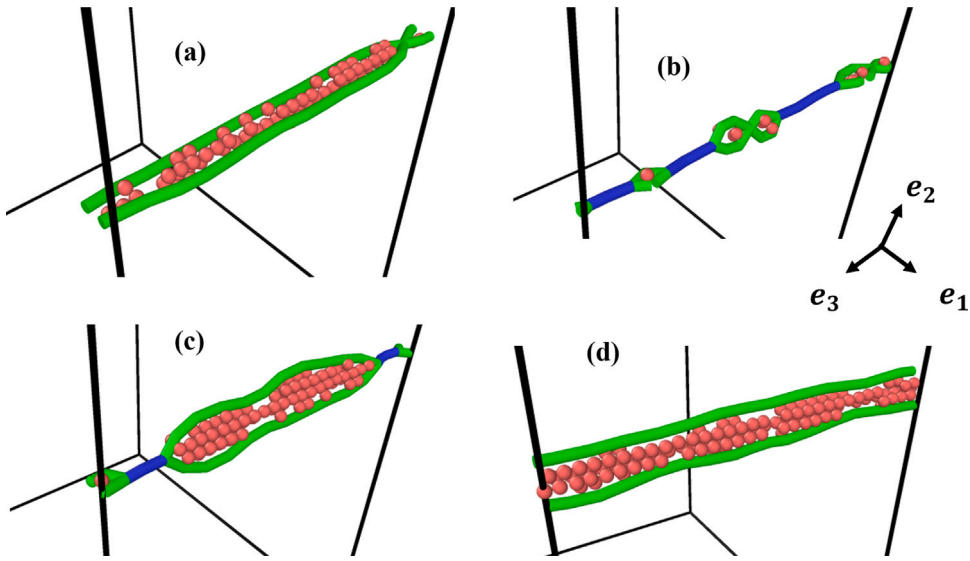
Fig. 4. Atomistic snapshots extracted at different times during the simulation. The figures illustrate the motion of dislocation lines during the Friedel–Escaig mechanism ($\mathbf{A} = K_1 \mathbf{e}_1 \otimes \mathbf{e}_2$, $K_1 < 0$) of cross-slip for flexible (long segment) dislocations. (a) Shockley partials on ($\bar{1}11$) plane, (b) Recombination of partials, (c) Protrusion of partials on the cross-slip plane, (d) Shockley partials on (111) plane. Note that FCC atoms are omitted. Green lines depict partials and blue lines depict perfect screw dislocation. Orange atoms are in HCP coordination. Atoms in FCC coordination are omitted. Primary and cross-slip planes are ($\bar{1}11$) and (111) respectively.

We consider three elementary cases in this work. The first is where the pure Escaig stress on the glide and cross-slip plane is the main non zero component and is positive. In the second case the Escaig stress is negative, and in the third case Schmid stress on the cross-slip plane is the main non zero component. An appropriate assignment of $\mathbf{A}$ yields these stresses. Note that minor hydrostatic stresses ($\sigma_{11} = \sigma_{22} = \sigma_{33}$) are present in the material after equilibration under NVE ensemble at finite temperatures due to thermal expansion but their influence on the cross-slip phenomenon is negligible.

3.2.1. Friedel–Escaig (FE) mechanism

$\mathbf{A}$ is chosen to be $K_1 \mathbf{e}_1 \otimes \mathbf{e}_2$ resulting in the generation of stress σ_e^g. This also induces Escaig stress on CS plane σ_e^{cs} as seen from (7). The stacking fault width (SFW) is guided by the interaction between Shockley partials, stacking fault energy, internal stress from the images, and the dominant stress σ_{12}. The condition $K_1 < 0$, results in negative σ_e^g which promotes decrease in the width of the stacking fault ribbon on the glide plane which, in turn, favors cross-slip. This results in constriction of each partial which leads to the formation of a perfect screw dislocation followed by a further dissociation of that perfect dislocation into partials on the cross slip plane. The latter is oriented at an angle of $\theta = 70.53°$ with respect to the primary slip plane.

We investigated the effect of the dislocation line length on cross-slip. The shorter dislocation segment of $8|\mathbf{b}|$ (dimension of fundamental domain) along $\mathbf{e}_3$ follows the FE mechanism uniformly. This means that the recombination of partials happens along the entire dislocation line, uniformly leading to a perfect screw dislocation, which then cross-slips without bowing. On the other hand, for the longer dislocation segments $32|\mathbf{b}|$ and $60|\mathbf{b}|$, the partials recombine over a short segment of the full dislocation line and protrude partially into the cross-slip plane, forming constriction joints (points which separate partials from recombined screw dislocation). The two constrictions move apart along the dislocation line to complete the cross-slip process. Fig. 4 illustrates the mechanism and shows the corresponding transition state for a longer dislocation. Here, we observe a dynamic variant of the Friedel–Escaig (Bonneville and Escaig, 1979) mechanism, which incorporates dislocation breathing all along its length.

Next, we choose $K_1 > 0$ for the same choice of $\mathbf{A}$. In this case, the Escaig stress on the glide plane is positive which enlarges the intrinsic stacking fault area between the two partial dislocations on the primary slip plane. Under continued loading, the SFW increases until it starts interacting with a neighboring partial on the same ($\bar{1}11$) glide plane. This leads to constriction of the leading partial with the trailing partial of the image forming a perfect dislocation. The perfect dislocation then causes slip, immediately followed by re-dissociation into partials on the adjacent ($\bar{1}11$) glide plane, climbing upwards by one atomic layer. This double slip phenomenon continues as the deformation progresses. The mechanical twin boundary gradually propagates towards the end of a domain under the shear strain produced during the loading. This results in twin boundary motion mediated by the creation, motion and annihilation of steps. Fig. 5 shows the temporal sequence of snapshots illustrating the mechanism for a small dislocation line length. In this case the imposition of periodic boundary conditions, in addition to the particular loading orientation used for high rate motion, also have an important effect on the pathway chosen and avoidance of stress buildup by cross-slip.
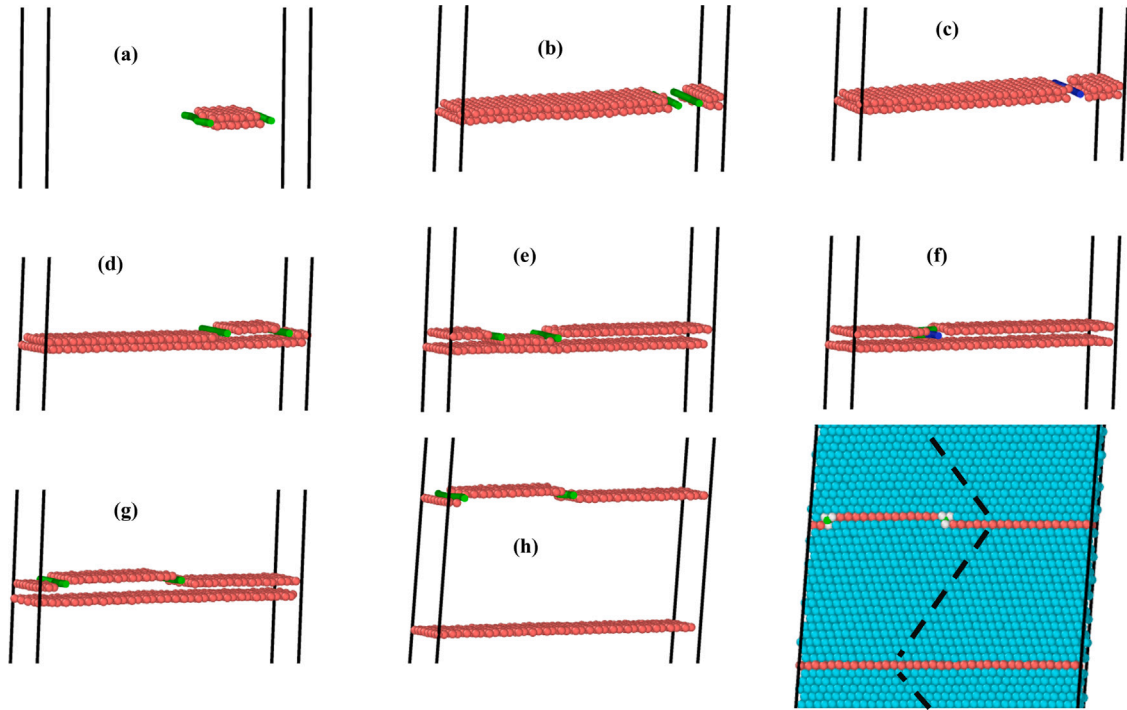
Fig. 5. Atomistic snapshots illustrating formation of thickening mechanical twin and the motion of dislocation lines during the multiple cross-slip of shorter dislocation segments when $\mathbf{A}$ is chosen to be $\mathbf{A} = K_1 \mathbf{e}_1 \otimes \mathbf{e}_2, K_1 > 0$. (a) Shockley partials intervening stacking fault on $(\bar{1}11)$ plane, (b) Enlargement of stacking fault area, (c) Formation of perfect dislocation, (d) Redissociation into partials on the adjacent glide plane, (e)–(g) Reiteration of events (b)–(d), (h) Formation of thicker mechanical twin. Cyan and orange colored atoms are in FCC and HCP coordination respectively. Blue and green lines depict perfect screw and partial dislocations respectively.

3.2.2. Fleischer mechanism

In this case we take the same initial conditions but $\mathbf{A} = K_2 \, \mathbf{e}_1 \otimes \mathbf{e}_3$ with $K_2 > 0$ or $K_2 < 0$, which generates the stress σ_s^{cs}. Contrary to the previous cases, the stacking fault width does not vary much due to absence of an Escaig stress. After some time, one partial dissociates into a stair-rod dislocation – a pure edge dislocation whose Burgers vector does not lie on the primary or cross-slip plane – and a Shockley partial which bows out into cross-slip plane. This is followed by the reaction of remaining partial in the primary plane with the stair-rod, forming a glissile trailing partial on the CS plane. As in cases above, only part of the dislocation bows out into CS plane for the longer flexible dislocations, whereas the shorter dislocations dissociate uniformly along their entire line length. The core structure of the activated dislocation undergoing cross slip contains a three-dimensional stacking fault structure as shown in Fig. 6 (cf., Fleischer (1959)).

We also conducted simulations under mixed loading conditions. This is achieved by sampling phase space where both K_1 and K_2 are non zero ($\mathbf{A} = K_1 \, \mathbf{e}_1 \otimes \mathbf{e}_2 + K_2 \, \mathbf{e}_1 \otimes \mathbf{e}_3$). It was observed that under mixed loading in the high-strain rate regime ($K_1, K_2 \approx 10^7$ s^{-1}), a combination of the FE and FL mechanisms may occur where part of the dislocation cross-slips by one mechanism and is completed by the other. The mechanism is illustrated in Fig. 7 where cross-slip initiates by constriction of partials into a finite length screw and is later assisted by formation of stair rod dislocation at the intersection of the primary and cross-slip planes. In some cases of mixed loading, initiation happened by the FL mechanism and in others, a mixture of perfect and stair rod dislocations appears at an initial stage.

In summary, we report four observed dynamical pathways in these highly non-equilibrium situations. In the range of conditions studied, cross-slip occurs via the acute variant (i.e., the angle between the glide direction in the cross-slip and the primary plane is acute) which is known to have lower activation energy. The FE mechanism operates when σ_e^g is the only non-zero dominant stress component and its direction is such that it reduces the separation between two partials on the glide plane. Hence the sign of σ_e^g is relevant. On the other hand, the Fleischer mechanism operates in the regime where σ_s^{cs} is non-zero and is independent of the direction of stress (i.e., the sign of K_2). This is consistent with earlier work where the dependence of the energy barrier for cross-slip on σ_s^{cs} is predicted to be quadratic (Kuykendall et al., 2020). Moreover, the mechanism we observed for a given shear loading remains independent of the strain rate, K_1, K_2 varying within four orders of magnitude (from 5×10^4 s^{-1} to 10^8 s^{-1}). (Simulations with lower strain rates are computationally demanding especially with the bigger fundamental domains of simulated atoms.)

We also explored the effect of dislocation line length on cross-slip. The preferred pathway is seen to remain invariant with respect to the length of the dislocation ranging from 8|$\mathbf{b}$| to 60|$\mathbf{b}$|. This finding is invariant with respect to different domain sizes considered in this work. This is in contrast to the finding reported in the literature where only the Fleischer mechanism was observed for
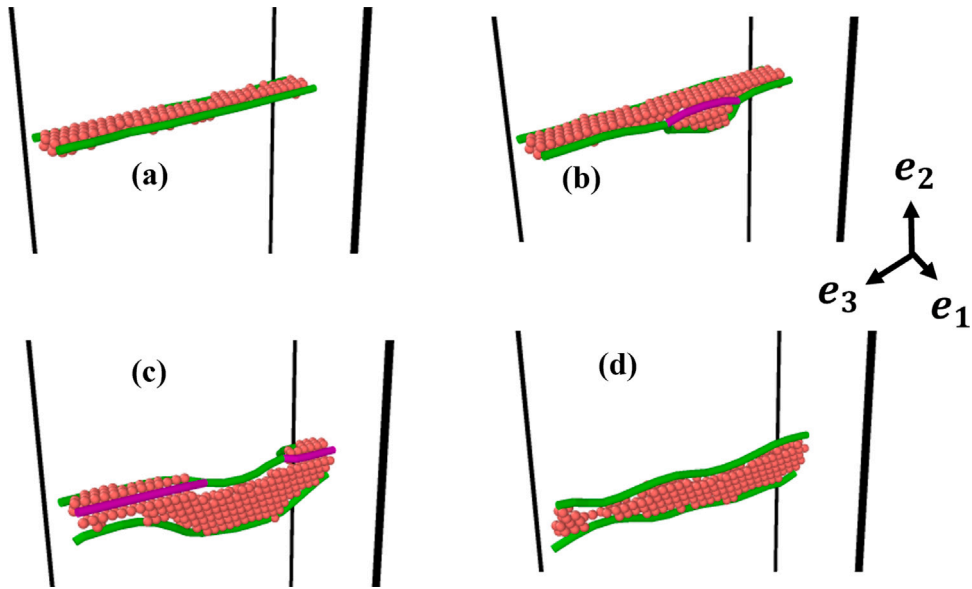
Fig. 6. Evolution of atomistic snapshot illustrating motion of dislocation lines during the Fleischer mechanism ($\mathbf{A} = K_2 \; \mathbf{e}_1 \otimes \mathbf{e}_3$ with $K_2 > 0$) of cross-slip for flexible dislocations. (a) Shockley partials on $(\bar{1}11)$ plane, (b) Dissociation of partial into stair-rod dislocation and leading partial which bows into cross-slip plane, (c) Protrusion along complete dislocation line length, (d) Shockley partials on (111) plane. Pink and green lines depict stair rod and partial dislocations respectively.
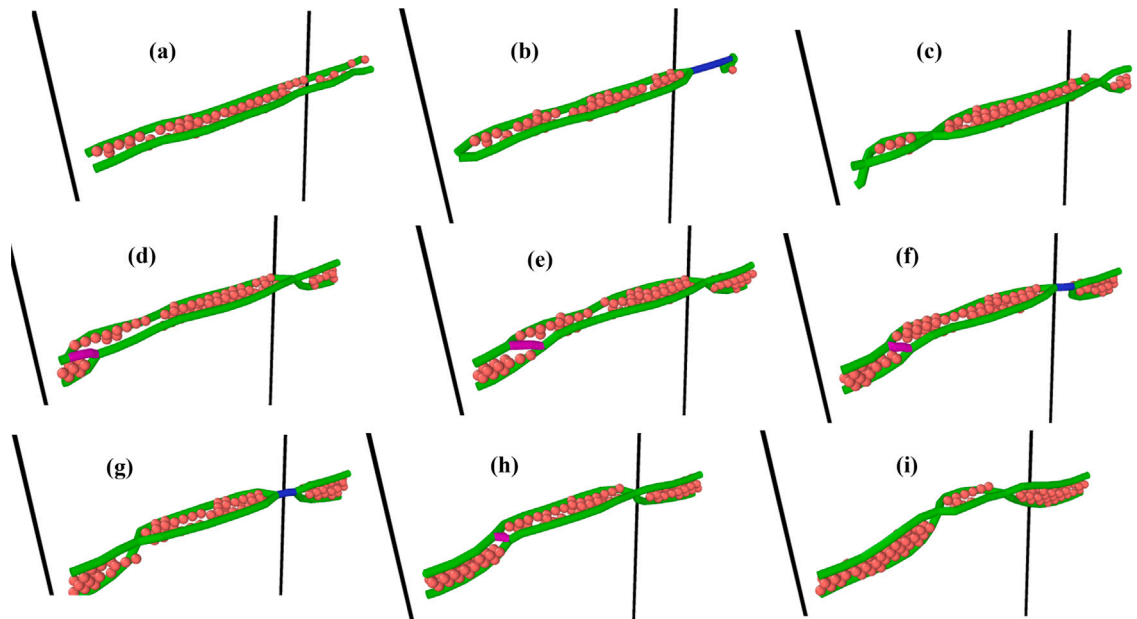

Fig. 7. Atomistic snapshots illustrating motion of dislocation lines during the mixed mechanism of cross-slip for flexible dislocations. The choice of $\mathbf{A}$ is given by ($\mathbf{A} = K_1 \; \mathbf{e}_1 \otimes \mathbf{e}_2 + K_2 \; \mathbf{e}_1 \otimes \mathbf{e}_3$). (a) Shockley partials on $(\bar{1}11)$ plane, (b) Recombination of a small segment of partials into the perfect screw, (c) Cross-slip of a small segment of partials, (d)–(e) Formation of stair-rod dislocation, (f) The transition state has mixed behavior where both stair-rod and perfect dislocation segments are present, (g)–(i) Further progression of cross-slip via mixed mechanism. .

shorter dislocation segments under constant stress at low temperatures of ~10K (Xu et al., 2017). Furthermore, Xu et al. (2017) use an NPT statistical ensemble with the Parrinello-Rahman barostat which samples the equilibrium time-invariant probability distribution at constant stress and temperature in contrast to OMD. A similar conclusion was made using NEB calculations in Al at zero temperature (Jin et al., 2011). However, we find that the dislocation length has a strong effect on the critical stress for cross-slip for a particular mechanism. This will be further investigated in the next section.
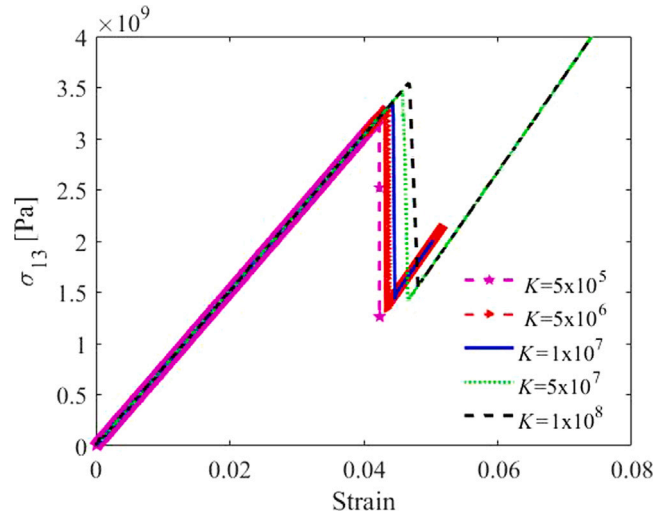
Fig. 8. Stress–strain response under different strain rates for the system undergoing cross-slipping by Fleischer mechanism ($\mathbf{A} = K\,\mathbf{e}_1 \otimes \mathbf{e}_3$ with $K > 0$.

3.3. Effect of strain rate and temperature on the critical stress for cross-slip

In this subsection we focus on the Fleischer mechanism and investigate the effect of strain rate and temperature in the large strain-rate regime. Fig. 8 shows the typical stress–strain response of the material at different strain rates that vary from 5×10^5 to 1×10^8 s^{-1}. The stress–strain curve abruptly decreases after linearly increasing to a local maximum at the first transition from elastic to plastic deformation. When the dislocation cross-slips, unloading waves are released immediately, modifying the local state. This in turn results in the fall of the global stress. The shear modulus is obtained by linear fitting of the stress–strain curve when the strain is <0.03 in the elastic region. It is given by $G = 75$ MPa which is in agreement with the effective isotropic shear modulus predicted by theory (Kang et al., 2014; Scattergood and Bacon, 1975, 1982). Inspection of the stress–strain curve reveals that strain rates in this range during shear loading have little effect on the elastic phase of the stress–strain relationship and a modest effect on the plastic phase. An increase in the strain-rate increases the local peak stress. This peak shear stress coincides with the stress at which the material begins to undergo cross-slip. These simulations serve as clear evidence of the dependence of plastic yield on the rate of deformation.

An interesting question is whether the transition state theory (TST) is valid under these conditions of high rate deformation. We try to answer this here for dislocation cross-slip by making a direct comparison of predictions of OMD with TST. A few studies in the literature have used the TST approach in the context of dislocation-defect interaction (Fan et al., 2013), mobility of screw dislocation (Fan et al., 2012) and dislocation nucleation (Zhu et al., 2008). Originally, TST was developed for chemical reactions or diffusion of atoms (Eyring, 1935; Marcelin, 1915). Vineyard (1957) later generalized this theory for multibody systems. A general multiscale method based on TST was formulated by Voter et al. (2002). TST determines the rate at which system at equilibrium jumps between two metastable basins by crossing the saddle region. Generally, one could question whether our system of dislocations stays in a basin for a sufficiently long time so as to reach a macroscopic equilibrium described by the formulas of equilibrium statistical mechanics, but we press ahead and evaluate it anyway. This transition rate at temperature T and effective stress σ is then expressed as

$$v = \tilde{v} \exp\left(\frac{-G_c(\sigma, T)}{k_B T}\right), \tag{8}$$

where $\tilde{v}$ is a frequency prefactor, G_c is the activation Gibbs free energy for cross-slip and k_B is Boltzmann constant (Ryu et al., 2011). The activation enthalpy H_c and activation entropy S_c are assumed to be insensitive to temperature under the range considered and G_c is defined by

$$G_c(\sigma, T) = H_c(\sigma) - T S_c(\sigma)$$

The cross-slip rate can be rewritten as

$$v = \tilde{v} \exp\left(\frac{S_c(\sigma)}{k_B}\right) \exp\left(\frac{-H_c(\sigma)}{k_B T}\right). \tag{9}$$

Hence, the contribution of activation entropy is contained in the overall multiplicative factor $\exp(S_c(\sigma)/k_B)$. Harmonic transition state theory (HTST) simplifies the rate equation by assuming vibrations to be simple harmonic near the basin and saddle point. This leads to

$$v_{\text{HTST}} = v_1 \Pi_{i=2}^N \frac{v_i}{v_i'} \exp\left(\frac{-H_c(\sigma)}{k_B T}\right) \tag{10}$$

where ν_1 is the fundamental frequency, ν_i and ν_i' are eigenfrequencies of the ith mode of the original and transition state respectively. Under the framework of HTST, the entropic factor $\exp(S_c(\sigma)/k_B)$ is given by $\Pi_{i=2}^{N} \frac{\nu_i}{\nu_i'}$ if $\tilde{\nu}$ is considered to be ν_1. The activation entropy is typically approximated using an empirical thermodynamic compensation law, or the Meyer–Neldel (M–N) rule which accounts for anharmonic effects such as temperature dependence of shear modulus, thermal expansion, and surface energies (Ryu et al., 2011; Meyer and Neldel, 1937). It is based on the empirical observation that the activation entropy is proportional to the activation enthalpy and is given by

$$S_c(\sigma) = \frac{H_c(\sigma)}{T_m} \tag{11}$$

where T_m is the melting temperature. We use the M–N rule to reduce the cross-slip rate to

$$\nu = \tilde{\nu} \exp\left(\frac{-H_c(\sigma)(1 - \frac{T}{T_m})}{k_B T}\right), \tag{12}$$

where G_c is taken to be $G_c(\sigma, T) = (1 - T/T_m)H_c$ in (8) under a first approximation of the effect of temperature on the activation free energy. Esteban-Manzanares et al. (2020) has shown the applicability of the M–N rule for aluminium within NPT dynamics of cross-slip via the Friedel–Escaig mechanism in a temperature range of 400–600 K.

The average critical stress for cross-slip is derived using the survival probability in an initial elastic bulk solid (Zhu et al., 2008), and is given by

$$\frac{\mathrm{d}f(t)}{\mathrm{d}t} = -\nu f(t),$$

where ν is given by (12). Our loading can be considered a constant engineering shear strain rate K applied to the solid. It can be seen from Fig. 7 that before the onset of cross-slip, the relationship between stress and strain remains linear and the shear modulus is insensitive to strain rate and temperature. Thus in the linear elastic deformation regime before cross-slip, the state of stress becomes time-dependent and is given by $\sigma = GKt$, where K is the shear rate. Following Fan et al. (2012), this can be used to make a change of variables which yields

$$\frac{\mathrm{d}f(\sigma)}{\mathrm{d}\sigma} = -\frac{\nu}{GK}f(\sigma), \qquad f(\sigma) = \frac{\exp\left(-\int_0^{\sigma}(\nu(\sigma')/GK)\mathrm{d}\sigma'\right)}{C}, \tag{13}$$

where $p(\sigma) = -\frac{df(\sigma)}{d\sigma} = \frac{1}{C}\frac{\nu(\sigma)}{GK}\exp\left(-\int_0^{\sigma}(\nu(\sigma')/GK)\mathrm{d}\sigma'\right)$ is the first escape probability distribution and C is normalization factor given by

$$\int_0^{\sigma_c} p(\sigma)d\sigma = 1 \;\Rightarrow\; C = \int_0^{\sigma_c} \frac{\nu(\sigma)}{GK} \exp-\int_0^{\sigma}(\nu(\sigma')/GK)\mathrm{d}\sigma' d\sigma. \tag{14}$$

Here, cross-slip is being treated as a probabilistic event. Thus, the critical stress obtained follows a distribution associated to repeated computational tests. The expected critical stress is achieved by taking first moment of the escape probability distribution:

$$\sigma_{(\text{avg})} = \int_0^{\sigma_c} \sigma p(\sigma)d\sigma = \frac{\int_0^{\sigma_c} \sigma\nu(\sigma)\exp\left(-\int_0^{\sigma}(\nu(\sigma')/GK)d\sigma' d\sigma\right)}{\int_0^{\sigma_c} \nu(\sigma)\exp\left(-\int_0^{\sigma}(\nu(\sigma')/GK)d\sigma' d\sigma\right)} \tag{15}$$

Eq. (15) predicts the TST guided temperature and shear rate dependence of the critical slip stress at a given activation enthalpy H_c. Note that since the material undergoes a linear elastic deformation before cross-slip, the constant stress and constant strain ensembles are equivalent here; either choice of independent variable could be used to find $\sigma_{(\text{avg})}$.

Several studies in the literature have estimated the contribution of the stress to the energy barrier associated with different mechanisms of cross-slip (Esteban-Manzanares et al., 2020; Kuykendall et al., 2020). We use the energy barrier proposed by Kuykendall et al. (2020), based on a modified string method for homogeneous cross-slip by Fleischer mechanism as a function of Escaig and Schmid stress acting on glide and cross-slip plane. This is given by

$$H_c(\tilde{\sigma}) = A[1 - (\frac{\tilde{\sigma}}{\sigma_c})^p]^q, \qquad \tilde{\sigma} = C_e^g\sigma_e^g + C_e^c\sigma_e^c + (D_s^c\sigma_s^{cs})^2, \tag{16}$$

where an external stress $\tilde{\sigma}$ lowers the energy barrier corresponding to cross-slip. In this comparison, we focus on the effect of Schmid stress on cross-slip plane σ_s^{cs} (corresponding to $\mathbf{A} = K\mathbf{e}_1 \otimes \mathbf{e}_3$) on the average critical flow stress σ_{13}^*. Thus, we reparameterize the activation barrier as

$$\sigma_e^g = \sigma_e^{cs} = 0, \qquad \sigma_s^{cs} = \frac{2\sqrt{2}}{3}\sigma_{13} \;\Rightarrow\; H_c(\sigma_{13}) = A[1 - (\frac{\sigma_{13}}{\sigma_c'})^{p'}]^{q'}, \tag{17}$$

where $A = 2.2352$ eV, $\sigma_c' = 3.3478$ GPa, $p' = 1.4576$ and $q' = 1.4428$. This is substituted into (15) to obtain the TST-based average theoretical critical stress σ_{13}^*.

In Fig. 9(a) we compare the variation of critical stress vs. strain rate for shorter dislocation segments at a constant temperature of 320 K and, in Fig. 9(b), vs. temperature at a constant strain rate of 10^7s^{-1}. Fig. 10 illustrates a similar variation of flow stress

for longer dislocations. Different choices of domain reproduce effectively the similar critical stress within statistical uncertainty. This shows the negligible impact of dislocation replicas on the behavior of the system. The critical stress does not show a large variation in the range investigated. This is consistent with the nature of the energy barrier which is found to be less sensitive to σ_s^{cs} as compared to other stress components (Kuykendall et al., 2020).

It is novel that the predictions of OMD are in reasonable agreement with those of TST for the constant value of $\bar{\nu}$ taken to be 6.7×10^{12} and 1×10^9 s^{-1} for shorter and longer segments respectively under high-rate deformation. These estimates are less than the Debye frequency, as expected. As dislocations become longer, the critical stress for cross-slip increases at all temperatures and strain rates. We conclude that the frequency prefactor is approximately inversely proportional to the length of the dislocation. This is consistent with the analysis by Friedel (2013) and Sobie et al. (2017) who predicted using a line tension model that the fundamental frequency of dislocations exhibits inverse dependence on the length. Thus, relatively short dislocation segments are activated for cross-slip more quickly than longer segments. Moreover, for a constant strain rate and temperature the temperature and strain-rate sensitivity of the critical stress decreases with an increase in the length of the dislocation.

We see that for a given temperature, deviations from the thermal activation stress begin appearing at strain rates which exceed a certain critical strain rate K^*. Evidently, this happens when the strain rate is so high that cross-slip is no longer thermally activated in that regime and it is purely stress driven. Therefore, the stress is being ramped up in the system until the athermal limit is reached. K^* is seen to be higher for shorter segments as compared to longer ones and is also a function of temperature of the system. For a given system, decreasing the temperature lowers this critical strain rate, allowing sufficient time for the dislocations to overcome the barrier via thermal assistance, and this time is inversely proportional to the temperature. However, the same system at higher temperatures for the same strain rate can be thermally activated. Similarly, we see that for a given shear rate, as the temperature decreases, there is an overshoot of the critical stress which correlates well with the suppression of thermal activation. This discrepancy is present in systems with different dislocation sizes, but it is more noticeable and it kicks in earlier, at a higher temperature, for the longer ones as compared to shorter segments. On the other hand, for all temperatures higher than T^*, the agreement is surprisingly good. Thus, a system can be divided into two regimes: (1) thermally activated and (2) athermal/stress driven, based on critical strain rate K^* at a given temperature T. Similarly for a sufficiently small shear rate K, a similar transition happens at a critical temperature T^*. T^* shifts towards a higher value as K increases. However, we want to point out that the deviation is not very significant for this system, and hence both regimes can still be approximated as thermally activated regimes for the development of constitutive rules for higher-scale models.

These results can be useful for the calibration of mesoscopic dislocation dynamics (DD) methods at high strain rates. DD methods employ physics-based constitutive rules for the motion of dislocations. An activated theory-based probability model has been used to incorporate cross-slip in DD simulations, but different studies have adopted different choices of the effective activation energy barrier (Kubin et al., 1992; Hussein et al., 2015; Longsworth and Fivel, 2021). The study conducted here provides confidence on the usage of an Escaig/Schmid stress dependent energy barrier for the modeling of cross-slip of screw dislocation segments under high rate deformation. It is an important finding that the frequency prefactors $\bar{\nu}$ obtained in this study for both longer and shorter segments are smaller than the ones typically reported for the similar system under equilibrium at some constant stress σ and temperature T (Esteban-Manzanares et al., 2020; Kuykendall, 2016). This suggests that higher strain rates lead to suppression of cross-slip. This is in agreement with the understanding that under large strain rates, thermal fluctuations become less efficient, i.e., the critical stress of cross-slip corresponds to an effective temperature which is smaller than actual one (Kubin, 2013). This can significantly affect the macroscopic response of system and can result in widely different behavior as compared to system under quasi-static loading. Thus, this work promotes the inclusion of appropriate strain-rate dependence of frequency prefactors for mesoscale modeling. The investigation also allows us to understand the transition from homogeneous cross-slip, seen for short dislocation segments, to inhomogeneous slip for larger dislocation lengths.

The frequency prefactor we obtain for the shorter segments might be an under estimate. This is owing to the fact that the activation barrier we use here for both our studies of shorter and flexible dislocations was originally derived for longer segments. In some prior studies, e.g. Rasmussen et al. (2000), the barrier is found to rise proportionally to the dislocation length for short dislocation segments and it saturates at constant value for sufficient long dislocations.

4. Unlubricated sliding

Friction is one of the most common phenomenon encountered in everyday life, and yet is one of the least understood physical phenomena. In this section, we briefly show that how OMD can be used to conduct sliding simulations which can help to investigate non-equilibrium processes occurring at the atomistic scale. The purpose of this section is to show an unexpected capability of our method, and also to see the formation of dislocations in a frictional sliding simulation. A comprehensive study of the physics of frictional sliding based on OMD will be presented elsewhere.

The technical details on the design of our OMD computational method for frictional sliding is, apart from initial conditions, almost the same as used above (For detailed information on the implementation, see Pahlani et al. (2022a)). In these simulations, it is more informative to adopt Lagrangian approach and follow the motion of simulated atoms which are defined at $t = 0$. To achieve that, we do not perform any remapping and redefinition of simulated atoms, and therefore they are free to leave or enter the fundamental domain. This requires a slight modification in our approach for the neighbor search implemented in Pahlani et al. (2022a). In the cell list method (Allen and Tildesley, 2017) we divide the fundamental domain into cells; all atoms are assigned to the cells according to their positions. In the present case we can have simulated atoms outside the fundamental domain (Fig. 11(b)); each of those exterior simulated atoms is assigned a cell based on the position of its corresponding non simulated atom that lies
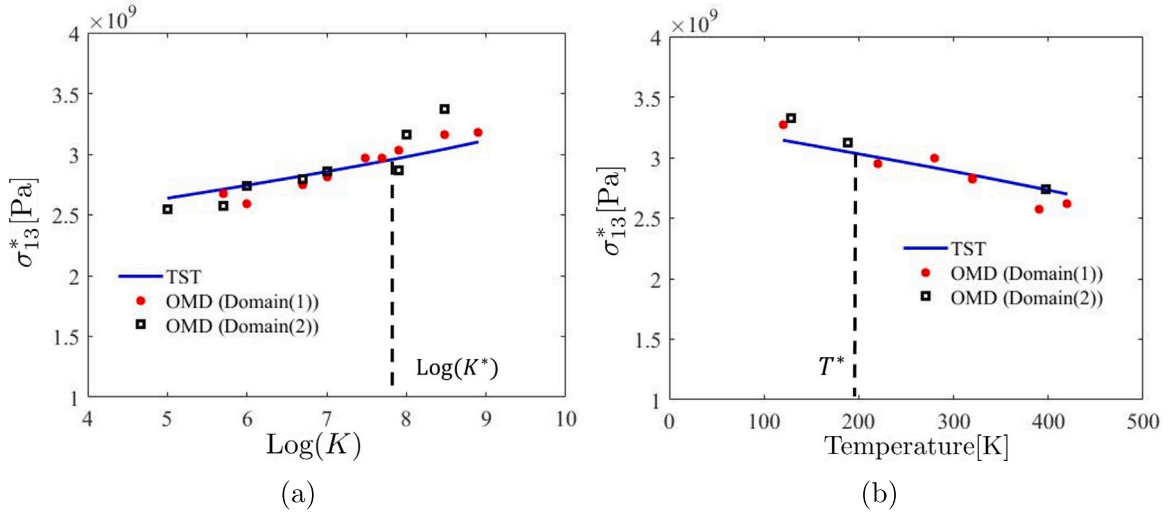
Fig. 9. Critical stress of cross-slip as a function of (a) logarithm of strain rate and (b) temperature for short dislocation segments undergoing cross-slip by the Fleischer mechanism.
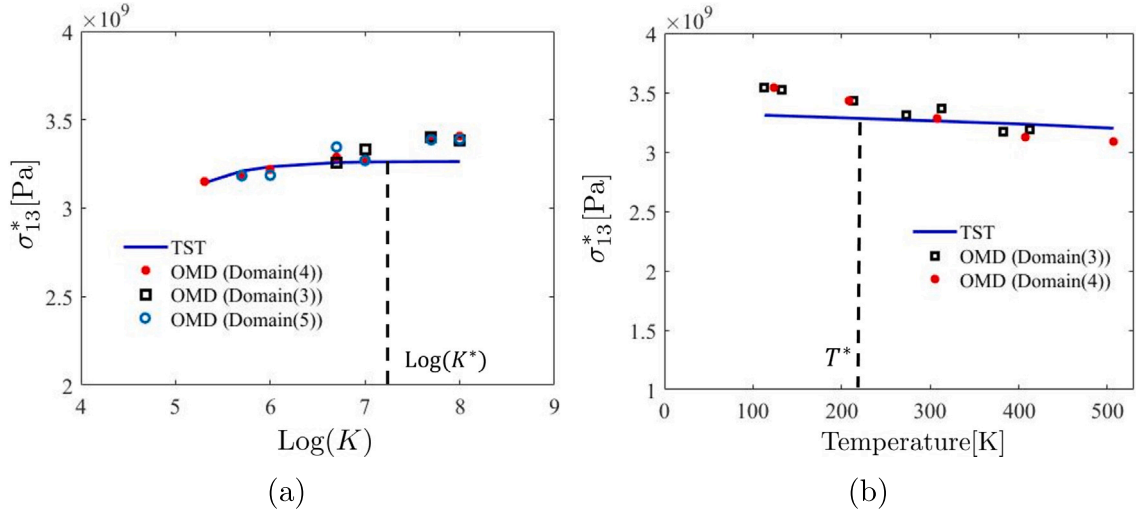

Fig. 10. Critical stress of cross-slip as a function of the (a) logarithm of strain rate and (b) temperature, for long and flexible dislocation segments undergoing cross-slip by the Fleischer mechanism.

inside the fundamental domain. That cell identifier is then used to find the atoms in the neighboring 27 cells which can interact with that atom. After this, we follow the same procedure which was used earlier to find the nearest image. The distance between simulated atoms $1, k$ and $1, m$ at time t can be written as:

$$\mathbf{r}_{k,m} = \mathbf{y}_{1,k} - \mathbf{y}_{1,m} = \{\lambda_1(\mathbf{I} + t\mathbf{A})\mathbf{e}_1 + \lambda_2(\mathbf{I} + t\mathbf{A})\mathbf{e}_2 + \lambda_3(\mathbf{I} + t\mathbf{A})\mathbf{e}_3\} \tag{18}$$

$\mathbf{r}_{k,m}$ is the shortest distance if and only if $|\lambda_i| \leq 0.5$. If $|\lambda_i| > 0.5$ then either simulated atom $1, k$ or simulated atom $1, m$ lies outside the domain. Atom $1, k$ then interacts with an image of the simulated atom $1, m$, and the distance between them is given by $\mathbf{r}_{k,m} - \lfloor(\lambda_i)\rfloor(\mathbf{I}+t\mathbf{A})\mathbf{e}_i$ where $\mathbf{r}_{k,m}$ is known from the calculation above and $\lfloor x \rfloor$ is the closest integer greater than or equal to x. This is repeated for each simulated atom whether it lies outside or inside the domain. Based on these computed interatomic distances, we calculate the force and then evolve the trajectory. We emphasize that both the implementation with remapping/redefinition used above, or the implementation used here are exact OMD methods.

The setup for the MD simulations of sliding is illustrated in Fig. 11. The system consist of two slabs. Both upper and lower slab are made of Argon atoms which interact via Lennard-Jones (LJ) potential. The two body interaction between atoms i and j is given by

$$\phi(r_{ij}) = 4\epsilon_{\text{LJ}}[(\frac{\sigma_{\text{LJ}}}{r_{ij}})^{12} - (\frac{\sigma_{\text{LJ}}}{r_{ij}})^6] \tag{19}$$

where $\sigma_{LJ} = 3.4 \times 10^{-10}$ m and $\epsilon_{LJ} = 1.65 \times 10^{-21}$ J. Basic physical properties are expressed in LJ units: σ_{LJ}, ϵ_{LJ}, ϵ_{LJ}/k_b, $\epsilon_{LJ}/\sigma_{LJ}^3$, $[m\sigma_{LJ}^2/\epsilon_{LJ}]^{1/2}$ for length, energy, temperature, pressure and time respectively. An FCC crystal is (presumably) the ground state of this potential with a lattice constant of $a = 1.556\,\sigma_{LJ}$. We use a computational domain containing 69 790 simulated atoms. The two slabs are specified by adding random noise to the positions of atoms at the mid plane along $\mathbf{e}_2$. We want to emphasize that the only essential difference between these simulations and the ones above involving dislocations (or those involving hypersonic flows of fluids Pahlani et al., 2021, 2022b) is a change of initial conditions.

Besides the random noise at the interface, the system is otherwise initialized using random velocities sampled from Maxwell–Boltzmann distribution at the initial temperature T_0 and further equilibrated to a steady state by running it under an NVE ensemble achieved by using OMD with $\mathbf{A} = 0$. The equilibrated system is illustrated in Fig. 11(a) where red and blue colored atoms simply highlight the slabs above and below the initially perturbed layer and aid in showing where the atoms go (The coloring is Lagrangian.) Next, we begin the OMD simulation under simple shearing by choosing $\mathbf{A} = K_1 \mathbf{e}_1 \otimes \mathbf{e}_2$ in the basis $\mathbf{e}_1 = [100], \mathbf{e}_2 = [010]$ and $\mathbf{e}_3 = [001]$, where $\mathbf{e}_1, \mathbf{e}_2$ defines the sliding plane.

The perturbed layer quickly evolves to an well-defined interface along which the two blocks slide as a frictional system, Fig. 11(b). Note that the portion of these slabs which is composed of non-simulated atoms is omitted from the visualization; only simulated atoms are shown. (The full set of atoms satisfying the equations of molecular dynamics fills all of space.) Frictional sliding can give rise to the generation of elastic shear waves at the interface in the fundamental domain and their images under the translation group. To minimize shear wave reverberations, fundamental domain and the value of the K_1 needs to be big enough such that the duration of the simulation is well within the propagation time of shear wave based on the macroscopic shear wave velocity and the size of the fundamental domain.

Fig. 11(c) gives insight into the deformation process; atoms in FCC coordination are omitted in Fig. 11(c). At first, perfect stair rod and mixed dislocations nucleate under the mid plane. The dislocations are identified using the same DXA algorithm within Ovito that was used earlier. As sliding evolves, the Shockley partials cross slips, majorly dominant by the Fleischer mechanism (in the system investigated) followed by the propagation of stacking faults in the lower slab on the preferred close packed slip plane. The temperature of the system increases with time since there are no thermostats applied and the external work is being done on the system. The instantaneous temperature at time t is computed by:

$$T(t) = \frac{m}{3k_b N} \left[\sum_i^N (v_{1,i}'^2 + v_{2,i}'^2 + v_{3,i}'^2) \right] \tag{20}$$

where, $v_{j,i}'$ denotes the thermal velocity (difference between particle velocity and mean velocity) of particle i in direction $\mathbf{e}_j$, and k_b is the Boltzmann constant.

In Fig. 12(b) we plot the temperature profile across the material for the average relative speed between slabs of about 120 m/s. The profile is computed by partitioning the fundamental domain into bins in the $\mathbf{e}_2$ direction. The temperature in each bin is then computed by local averaging of the variance of kinetic energy of the atoms present in the bin. The temperature at the interface is highest and decreases monotonically. The temperature at the interface reaches approximately 48 K which gives rise to onset of melting and mechanical mixing at the interface.

Fig. 12(a) shows the evolution of sliding stress τ_{12}, computed using the Virial stress given by

$$\boldsymbol{\sigma}(t) = -\frac{1}{V} \left(\sum_{i=1}^N m_i (\mathbf{v}_i - \bar{\mathbf{v}}) \otimes (\mathbf{v}_i - \bar{\mathbf{v}}) + \sum_{j \neq i}^N \sum_{i=1}^N \mathbf{r}_{ij} \otimes \mathbf{F}_{ij} \right), \tag{21}$$

where N is the number of simulated atoms, $\bar{\mathbf{v}}$ is the mean velocity, $\mathbf{r}_{ij}$ is the inter-atomic distance, $\mathbf{F}_{ij}$ is the interatomic force between atom i and j and $\tau = \sigma - \frac{1}{3}\mathrm{tr}(\sigma)\mathbf{I}$. This stress increases elastically until the initiation of sliding, at which time the stress drops rapidly. The tangential stress can have a strong dependence on the velocity as described by Rigney and Hammerberg (1998). We also see that the sliding stress follows an oscillating behavior reminiscent of widely observed microscopic stick–slip behavior as the two slabs move past each other. During the 'stick' phase, both the slabs are stuck to each other. This is followed by sudden slip. Similar behavior is observed in the slab's velocity field as well. When the relative velocity between the blocks is small then materials can cold weld together. Conversely, if it is very high then sliding can occur at the junction between simulated and non-simulated atoms away from the interface, indicating a more general disintegration at these extremely high rates. These results indicate that, with an appropriate choice of $\mathbf{A}$ and initial conditions within the OMD framework, we are able to conduct high speed sliding studies at the molecular scale. Atomistic studies on sliding are usually performed by building reservoirs to apply external tangential force (Epiphaniou, 2010). On the other hand, in OMD since external macroscopic motion is applied to the domain through the imposition of linear transformation tensor $\mathbf{A}$, it avoids the need of building external reservoirs which simplifies the simulation to a great extent and saves computational time.

5. Conclusion

OMD provides a computational framework for the exploration of the interplay between motions at the continuum scale and atomic scale. The macroscopic affine motions simulated by OMD are exact solutions of macroscopic continuum mechanics, and, at atomic scale, every atom out to infinity, simulated or nonsimulated, satisfies the equations of molecular dynamics to high accuracy. Thus, OMD is an exact approach for doing NEMD arising from the invariance of underlying potential energy surfaces which originates from Born–Oppenheimer quantum mechanics. This motivates its usage to make connections with larger length and time scale theories which can improve mesoscopic and macroscopic predictions of realistic systems.
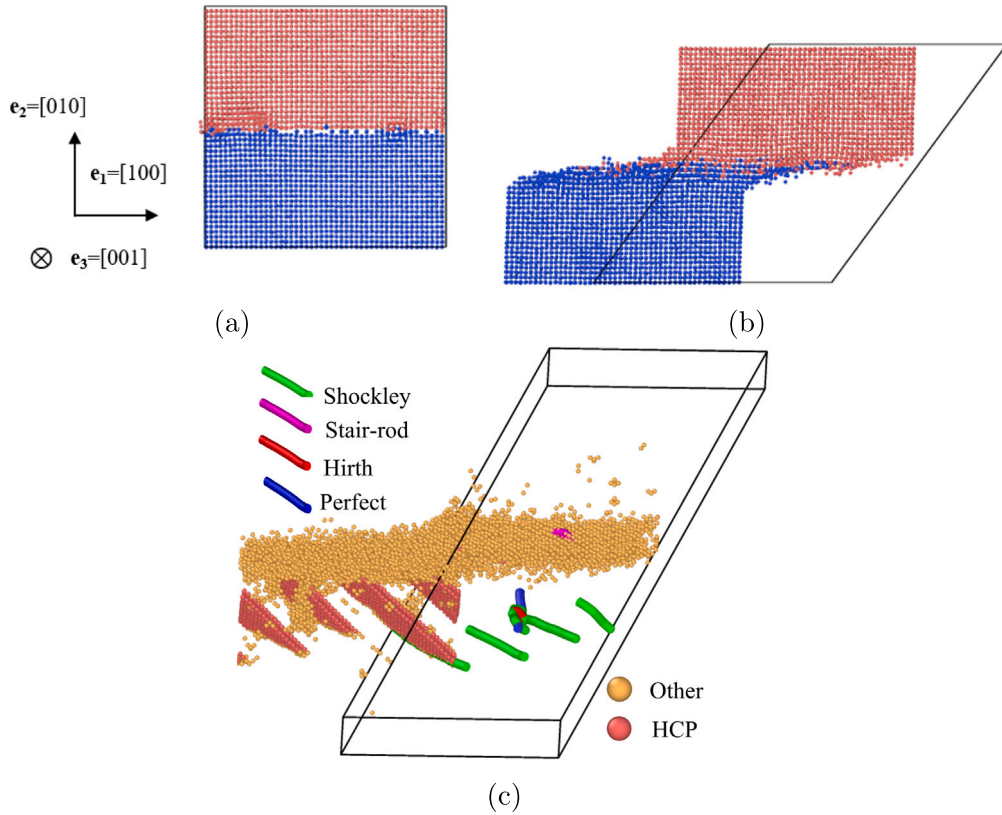
Fig. 11. Atomic configuration associated with the system at an (a) initial state and (b) during sliding. Red and blue colored atoms constitute two LJ slabs of simulated atoms. (c) Nucleation and motion of various dislocations in the lower slab during sliding.
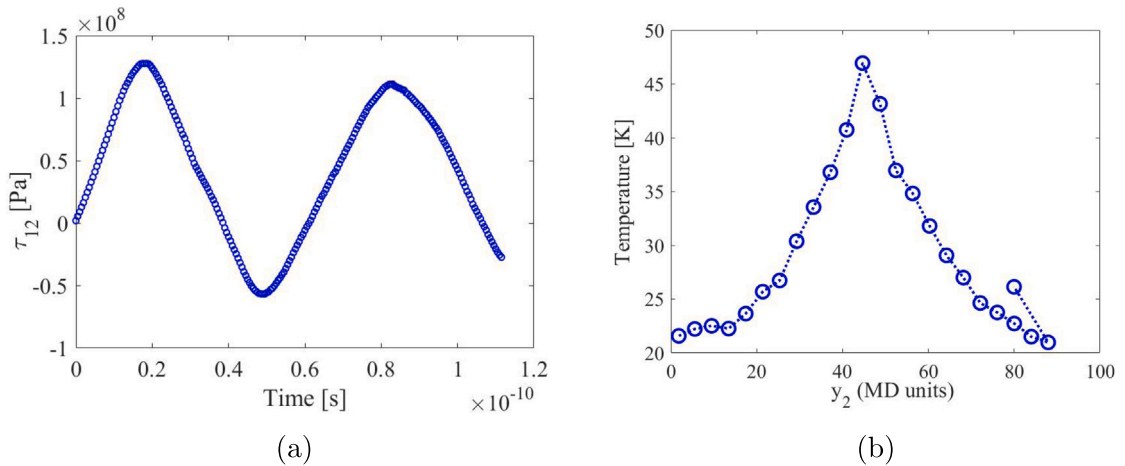

Fig. 12. (a) Evolution of sliding stress (b) Temperature profile across $\mathbf{e}_2$ direction. Dimension of the domain: 15.8 nm × 31.7 nm × 5.29 nm.

In this work, we focused on the modeling of cross-slip in a bulk crystal under high-rate loading. We are able to give a detailed description of the onset of cross-slip by Friedel–Escaig or Fleischer mechanisms under different macroscopic motions, and also the appearance of twinning and step motion. It is important to note that under mixed loading conditions, a combination of FE and FL mechanisms may also occur which is not commonly assumed in DD-based studies.

The OMD method provides a framework to develop a multiscale model to investigate the interplay between cross-slip stress, temperature, and strain rates. We propose an activated theory-based rule for the cross-slip stress as a function of strain rate and

temperature under high strain rates for the FL mechanism. Surprisingly, it was found that the response of the material under far-from-equilibrium conditions is consistent with an equilibrium theory of activation within a constant stress ensemble, under appropriate evaluations. The critical stress for cross-slip depends on the thermodynamic properties of activation, such as activation free energy, enthalpy and entropy. The use of a stress-dependent activation energy in conjunction with the empirical Meyer–Neldel rule for the entropic contribution captures the correct probabilistic behavior of the system across a wide range of shear rate and temperature. We also verified the general dependence of the activation energy on effective stress composed of Escaig and Schmid components purely based on the atomistic investigation. These findings can easily be incorporated into dislocation dynamics simulations to improve probabilistic models of bulk cross-slip.

Finally, we presented initial results of frictional sliding at high rates. Wave interactions with images could be avoided in these simulations without compromising the method. Dislocations formed initially at the interface and, under various conditions, we observed stick–slip, a temperature rise at the interface and, at extremely high rates, a type of fragmentation.

Taken together, a surprising aspect of this OMD implementation is that essentially the same numerical method, with the same atomic forces and same **A**, can be used to study diverse behavior such as slip, cross-slip by various mechanisms, twinning and step motion and frictional sliding, simply by changing the initial conditions. With earlier work, this universality extends to behavior in liquids and gases, and, with appropriate groups, to nanostructures.

CRediT authorship contribution statement

Gunjan Pahlani: Conceptualization, Methodology, Software, Formal analysis, Investigation, Writing – original draft, Writing – review & editing. **Ananya Renuka Balakrishna:** Conceptualization, Methodology, Software, Investigation, Writing – original draft, Writing – review & editing. **Richard D. James:** Conceptualization, Methodology, Formal analysis, Investigation, Resources, Writing – review & editing, Supervision, Project administration, Funding acquisition.

Declaration of competing interest

No conflict of interest.

Data availability

Data will be made available on request.

Acknowledgments

References

Abou-Sayed, A., Clifton, R., Hermann, L., 1976. Exp. Mech. 16 (4), 127–132.
Admal, N.C., Tadmor, E.B., 2010. J. Elasticity 100 (1), 63–143.
Aghaei, A., Dayal, K., 2011. J. Appl. Phys. 109 (12), 123501.
Aghaei, A., Dayal, K., Elliott, R.S., 2013. J. Mech. Phys. Solids 61 (2), 557–578.
Alder, B.J., Wainwright, T.E., 1959. J. Chem. Phys. 31 (2), 459–466.
Allen, M.P., Tildesley, D.J., 2017. Computer Simulation of Liquids. Oxford University Press.
Bernstein, N., Tadmor, E., 2004. Phys. Rev. B 69 (9), 094116.
Bonneville, J., Escaig, B., 1979. Acta Metall. 27 (9), 1477–1486.
Conti, S., Hauret, P., Ortiz, M., 2007. Multiscale Model. Simul. 6 (1), 135–157.
Dayal, K., James, R.D., 2010. J. Mech. Phys. Solids 58 (2), 145–163.
Dayal, K., James, R.D., 2012. J. Fluid Mech. 691, 461–486.
Dumitrică, T., James, R.D., 2007. J. Mech. Phys. Solids 55 (10), 2206–2236.
Epiphaniou, N., 2010. Modelling of Dynamic Friction Across Solid Material Interfaces Using Molecular Dynamics Techniques (Ph.D. thesis). Cranfield University.
Esteban-Manzanares, G., Santos-Güemes, R., Papadimitriou, I., Martínez, E., LLorca, J., 2020. Acta Mater. 184, 109–119.
Evans, D.J., Morriss, O., 1984. Comput. Phys. Rep. 1 (6), 297–343.
Eyring, H., 1935. J. Chem. Phys. 3 (2), 107–115.
Fan, Y., Osetskiy, Y.N., Yip, S., Yildiz, B., 2013. Proc. Natl. Acad. Sci. 110 (44), 17756–17761.
Fan, Y., Osetsky, Y.N., Yip, S., Yildiz, B., 2012. Phys. Rev. Lett. 109 (13), 135503.
Fleischer, R., 1959. Acta Metall. 7 (2), 134–135.
Friedel, J., 2013. Dislocations: International Series of Monographs on Solid State Physics, Vol. 3. Elsevier.
Hardy, R.J., 1982. J. Chem. Phys. 76 (1), 622–628.
Hardy, R.J., Root, S., Swanson, D.R., 2002. AIP Conf. Proc.. 620, (1), American Institute of Physics, pp. 363–366.
Hirel, P., 2015. Comput. Phys. Comm. 197, 212–219.
Hoover, W.G., Evans, D.J., Hickman, R.B., Ladd, A.J., Ashurst, W.T., Moran, B., 1980. Phys. Rev. A 22 (4), 1690.
Hull, D., Bacon, D.J., 2001. Introduction to Dislocations. Butterworth-Heinemann.
Hussein, A.M., Rao, S.I., Uchic, M.D., Dimiduk, D.M., El-Awady, J.A., 2015. Acta Mater. 85, 180–190.
James, R.D., 2006. J. Mech. Phys. Solids 54 (11), 2354–2390.
Jin, C., Xiang, Y., Lu, G., 2011. Phil. Mag. 91 (32), 4109–4125.

Kang, K., Yin, J., Cai, W., 2014. J. Mech. Phys. Solids 62, 181–193.

Kim, K., Clifton, R., 1980. Pressure-shear impact of 6061-T6 aluminum.

Kubin, L., 2013. Dislocations, Mesoscale Simulations and Plastic Flow, Vol. 5. Oxford University Press.

Kubin, L.P., Canova, G., Condat, M., Devincre, B., Pontikis, V., Bréchet, Y., 1992. Solid State Phenomena, Vol. 23. Trans Tech Publ, pp. 455–472.

Kuykendall, W., 2016. Investigating Strain Hardening by Simulations of Dislocation Dynamics (Ph.D. thesis). Stanford University.

Kuykendall, W.P., Wang, Y., Cai, W., 2020. J. Mech. Phys. Solids 144, 104105.

Lees, A., Edwards, S., 1972. J. Phys. C: Solid State Phys. 5 (15), 1921.

Longsworth, M., Fivel, M., 2021. J. Mech. Phys. Solids 153, 104449.

Madec, R., Devincre, B., Kubin, L., 2002. Scr. Mater. 47 (10), 689–695.

Marcelin, R., 1915. Ann. Phys. 3, 120–184.

Meyer, W., Neldel, H., 1937. Z. Tech. Phys. 18 (12), 588–593.

Miller, R.E., Tadmor, E.B., Gibson, J.S., Bernstein, N., Pavia, F., 2016. J. Chem. Phys. 144 (18), 184107.

Mordehai, D., Ashkenazy, Y., Kelson, I., Makov, G., 2003. Phys. Rev. B 67 (2), 024112.

Mordehai, D., Kelson, I., Makov, G., 2005. Mater. Sci. Eng. A 400, 37–39.

Oren, E., Yahel, E., Makov, G., 2016. Modelling Simul. Mater. Sci. Eng. 25 (2), 025002.

Oren, E., Yahel, E., Makov, G., 2017. Comput. Mater. Sci. 138, 246–254.

Pahlani, G., Schwartzentruber, T.E., James, R.D., J. Fluid Mech., (Invited Revisions).

Pahlani, G., Schwartzentruber, T.E., James, R.D., 2022a. J. Comput. Phys. 111938.

Pahlani, G., Schwartzentruber, T.E., James, R.D., 2022b. AIAA SCITECH 2022 Forum. p. 1012.

Pahlani, G., Torres, E., Schwartzentruber, T.E., James, R.D., 2021. AIAA Scitech 2021 Forum. p. 0707.

Parrinello, M., Rahman, A., 1981. J. Appl. Phys. 52 (12), 7182–7190.

Püschl, W., 2002. Prog. Mater. Sci. 47 (4), 415–461.

Rao, S., Parthasarathy, T., Woodward, C., 1999. Phil. Mag. A 79 (5), 1167–1192.

Rasmussen, T., Vegge, Leffers, T., Pedersen, O., Jacobsen, K.W., 2000. Phil. Mag. A 80 (5), 1273–1290.

Ravindran, S., Lovinger, Z., Gandhi, V., Mello, M., Ravichandran, G., 2020. Extreme Mech. Lett. 41, 101044.

Rigney, D., Hammerberg, J., 1998. Mrs Bull. 23 (6), 32–36.

Ryu, S., Kang, K., Cai, W., 2011. J. Mater. Res. 26 (18), 2335–2354.

Scattergood, R., Bacon, D., 1975. Phil. Mag. 31 (1), 179–198.

Scattergood, R., Bacon, D., 1982. Acta Metall. 30 (8), 1665–1677.

Siegel, D.J., 2005. Appl. Phys. Lett. 87 (12), 121901.

Sobie, C., Capolungo, L., McDowell, D.L., Martinez, E., 2017. Acta Mater. 134, 203–210.

Stukowski, A., 2009. Modelling Simul. Mater. Sci. Eng. 18 (1), 015012.

Stukowski, A., Albe, K., 2010. Modelling Simul. Mater. Sci. Eng. 18 (8), 085001.

Tadmor, E.B., Miller, R.E., 2011. Modeling Materials: Continuum, Atomistic and Multiscale Techniques. Cambridge University Press.

Tadmor, E.B., Phillips, R., Ortiz, M., 1996. Langmuir 12 (19), 4529–4534.

Thompson, A.P., Aktulga, H.M., Berger, R., Bolintineanu, D.S., Brown, W.M., Crozier, P.S., in't Veld, P.J., Kohlmeyer, A., Moore, S.G., Nguyen, T.D., et al., 2022. Comput. Phys. Comm. 271, 108171.

Vineyard, G.H., 1957. J. Phys. Chem. Solids 3 (1–2), 121–127.

Voter, A.F., Chen, S.P., 1986. MRS Online Proc. Libr. (OPL) 82.

Voter, A.F., Montalenti, F., Germann, T.C., 2002. Annu. Rev. Mater. Res. 32 (1), 321–346.

Xu, S., Xiong, L., Chen, Y., McDowell, D.L., 2017. Acta Mater. 122, 412–419.

Zhu, T., Li, J., Samanta, A., Leach, A., Gall, K., 2008. Phys. Rev. Lett. 100 (2), 025502.